Inorganic Chemistry

pubs.acs.org/IC

Article

Structural Features, Anisotropic Thermal Expansion, and Thermoelectric Performance in Bulk Black Phosphorus Synthesized under High Pressure

João Elias F. S. Rodrigues,* Javier Gainza, Federico Serrano-Sánchez, Carlos López, Oscar J. Dura, Norbert Nemes, Jose L. Martinez, Yves Huttel, Francois Fauth, Maria Teresa Fernández-Diaz, Nevenko Biškup, and José Antonio Alonso*

Cite This: https://dx.doi.org/10.1021/acs.inorgchem.0c01573

Read Online

ACCESS | Metrics & More | Article Recommendations | Supporting Information

ABSTRACT: Black phosphorus (BP) allotrope has an orthorhombic crystal structure with a narrow bandgap of 0.35 eV. This material is promising for 2D technology since it can be exfoliated down to one single layer: the well-known phosphorene. In this work, bulk BP was synthesized under high-pressure conditions at high temperatures. A detailed structural investigation using neutron and synchrotron X-ray diffraction revealed the occurrence of anisotropic strain effects on the BP lattice; the combination of both sets of diffraction data allowed visualization of the lone electron pair $3s^2$. Temperature-dependent neutron diffraction data collected at low temperature showed that the *a* axis (zigzag) exhibits a *quasi*-temperature-independent thermal expansion in the temperature interval from 20 up to 150 K. These results may be a key to address the anomalous behavior in electrical resistivity near 150 K. Thermoelectric properties were also provided; low thermal conductivity from 14 down to 6 $Wm^{-1}K^{-1}$ in the range 323−673 K was recorded in our polycrystalline BP, which is below the reported values for single-crystals in literature.

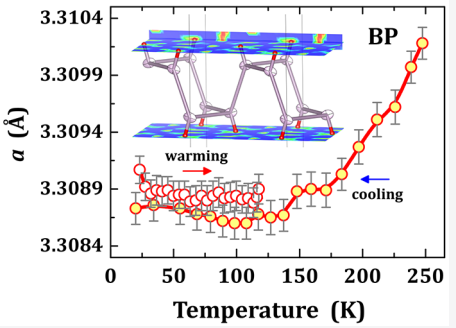

INTRODUCTION

Black phosphorus (BP) belongs to the class of layered materials, prone to exfoliation, which are now promising as two-dimensional (2D) systems for applications in nano- and microelectronic devices. Similar to graphite or transition-metal dichalcogenides MX_2 (M = Mo, W, V, Pt; X = S, Se, Te), BP presents a layered structure with unusual anisotropic properties. The black phosphorus allotrope has an orthorhombic crystal structure with a *Cmca* space group, containing puckered double layers stacked along the *b*-axis. Bulk BP is a direct bandgap ($E_g \sim$ 0.35 eV) and a natural *p*-type doped semiconductor, with a high carrier mobility of *ca.* 10^3−10^4 $cm^2V^{-1}s^{-1}$ at room conditions.[1] Similar to graphite, BP can be isolated as few layers of phosphorene ($E_g \sim 2$ eV) by mechanical exfoliation.[2] The direct bandgap at Γ-point can be tuned from 0.35 up to 2 eV depending on the number of layers.[3,4] The phosphorene stacking induces dispersion along the Γ−Z path, i.e., a narrow gap at Z-point is produced in bulk form.[5] These materials constitute a branch of 2D technology for the new generation of optoelectronics, field-effect transistors (FETs), photocatalysts, thermal imaging, etc.[1] Structurally, BP is stable under ambient pressure up to 823 K when it spontaneously evolves to the red phosphorus allotrope.[6]

Some synthesis routes are reported for preparing BP bulk samples, including mechanical milling,[7] chemical vapor transport,[8] recrystallization from mercury or bismuth, etc., in which white phosphorus may be used as starting precursor. The routes available are important for evaluating the final quality of the exfoliated BP flakes. Alternative methods consider the red phosphorus as a precursor but combined with some additives such as tin-based iodides or gold catalyst. The main hindrance for industrial applications lies in the secondary phase formation by additives and toxic chemicals which are almost impossible to eliminate. However, BP can also be synthesized directly from red phosphorus under high-pressure and high temperature,[9] typically 0.4 GPa and 853 K,[10] which leads to high quality BP flakes. The very first high-pressure synthesis of black phosphorus was carried out by Percy W. Bridgman, who used a pressure of 1.2 GPa at 473 K for 30 min directly from white phosphorus.[11,12] It is worth saying that the synthesis conditions may vary in different literature reports. The novel technologies in high-pressure apparatus, however, provided several options to produce BP, for instance, at room temperature under 10 GPa

Received: May 29, 2020

or even high energy ball milling, which typically leads to local pressures around 6 GPa and temperatures of 473 K.[13]

In the field of thermoelectricity, BP seems to be promising due to the elevated Seebeck coefficient of +335(10) μVK^{-1} for bulk samples near room temperature.[14] The Seebeck coefficient of bulk BP is almost isotropic even in single crystal samples.[15] Beyond that, theoretical studies predict zT values of 1.1 at high temperature, which could be enhanced by acceptor/donor Sb doping ($zT = 5$).[16] zT denotes the dimensionless Figure of Merit which accounts for the performance of thermoelectrics by balancing the electronic and lattice properties: $zT = S^2\sigma T/(\kappa_{ele} + \kappa_{lat})$ where σ and κ_{ele} are carrier electrical and thermal conductivities, respectively, while κ_{lat} is the lattice (or phonon) thermal conductivity and T is the absolute temperature. Up to now, however, few works were devoted to experimentally describe the thermoelectric properties in few-layer and bulk black phosphorus, including a deep characterization of the Seebeck, electrical, and thermal conductivities from room to high temperatures (at 773 K). The work by Hu et al.[17] deserves to be mentioned; he reported the low-temperature thermoelectric properties in BP single-crystal form. The authors argued that a long phonon mean free path is responsible for a large in-plane thermal conductivity of 180 Wm^{-1}K^{-1} at 25 K. Recently, the in-plane anisotropy of thermoelectric properties of BP was investigated in the temperature range 300−600 K in single crystals prepared by chemical vapor transport method.[15] The thermoelectric performance in polycrystalline BP was not addressed in depth so far.

In this work, we present a route to synthesize large pieces of bulk BP (polycrystalline) under high-pressure (HP) conditions at high temperatures directly from amorphous red phosphorus, without insertion of any additive. A combination of both neutron and synchrotron X-ray diffraction was essential to unveil the structural details and, mainly, the strain effects induced by HP conditions in our BP samples along with the location of the lone electron pairs 3s^2 of P atoms. Such a structural characterization was followed by neutron diffraction at low temperature, which demonstrated an anisotropic thermal expansion with *quasi*-temperature-independence through the zigzag direction. On the basis of these results, we rehash a discussion on the origin of an anomalous trend in the electrical resistivity of BP at low temperature. We also reported the high temperature thermoelectric performance in polycrystalline BP not yet reported in the literature. Particularly, low thermal conductivity from 14 down to 6 Wm^{-1}K^{-1} in the temperature range 323−673 K was obtained for our polycrystalline BP, which is below the literature values for single-crystals so far.

EXPERIMENTAL SECTION

High-Pressure Synthesis. Black phosphorus was synthesized using a high-pressure procedure in a piston−cylinder press (Rockland Research Co.) and a pressure of 2 GPa at a high temperature of 1073 K for 1 h. Initially, small pieces of amorphous red phosphorus (Alfa-Aesar) were ground in an agate mortar inside a nitrogen-filled glovebox; the material was sealed in a niobium capsule and then placed inside a cylindrical graphite heater. After being quenched and after the release of pressure, the hard pieces (6−7 mm in diameter; 5 mm in thickness) of BP were carefully polished for thermoelectric studies and also ground into fine powder for structural studies. First tests showed that our black phosphorus samples are perfectly exfoliable. The BP phase formation was first confirmed by laboratory X-ray diffraction (Cu Kα radiation; λ = 1.5418 Å) without signals of secondary phases, as represented in Figure 1a. Our first attempts to produce BP in gold capsules failed due to the stabilization of Au_3P_2 secondary phase. Nb was demonstrated to be ideal to yield pure BP without secondary phases.

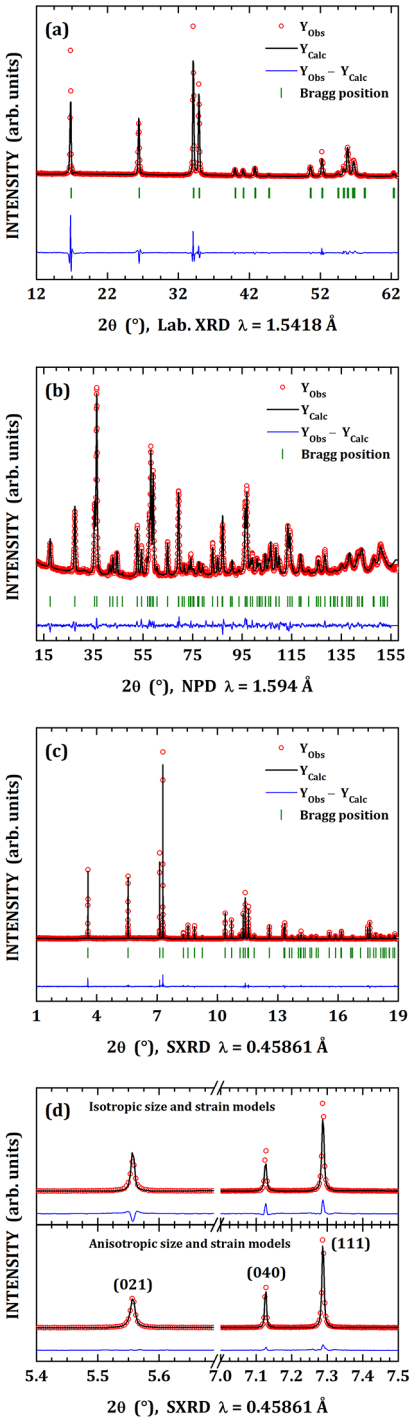

Figure 1. (a) Room temperature laboratory X-ray diffraction pattern of BP. (b) RT neutron powder diffraction of BP. (c) RT synchrotron X-ray pattern. (d) Details on the Rietveld refinement performed using both isotropic and anisotropic size/strain models. Red open circles represent the experimental data, the black line refers to the calculated profile, the blue line is the difference between experimental and calculated data, and dark green bars denote the Bragg reflections.

Structural Characterization. Structural characterizations were performed in powder samples. The synchrotron X-ray powder diffraction (SXRD) patterns were collected in the MSPD high resolution diffractometer at the CELLS−ALBA synchrotron, Barcelona (Spain), with an incident beam with 38 keV energy, λ = 0.45861 Å. The

https://dx.doi.org/10.1021/acs.inorgchem.0c01573
Inorg. Chem. XXXX, XXX, XXX−XXX

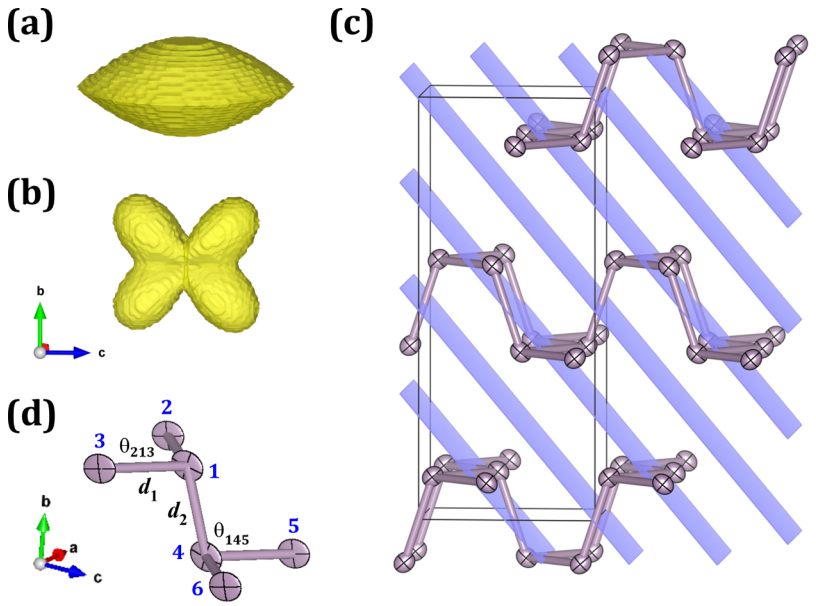

Figure 2. Anisotropic size (a) and strain (b) models employed during the Rietveld refinement from SXRD data. Crystalline planes (blue coloring) along (011) direction in which the strain effects are more significant (c). Unit cell is represented in panel c as black lines, forming a rectangular box. The strain direction is better represented by the (0, 2*n*, *n*) plane family. Sketch of the local structure of black phosphorus, exhibiting the definition of d_1, d_2, θ_{145}, and θ_{213} parameters (d).

high angular resolution mode (MAD setup) on the MSPD-diffractometer was utilized. The polycrystalline powder was contained in glass capillaries of 0.7 mm diameter, which were rotating during the acquisition time. The refinement of the structure was performed by the Rietveld method using the *Fullprof* software.[18] The following parameters were refined: zero-point error, scale factor, lattice parameters, atomic coordinates, and anisotropic displacement factors. The profile shape was modeled using the Thompson-Cox-Hastings pseudo-Voigt function, and the instrumental resolution parameters were considered in the refinements in order to obtain the microstructural parameters. Thus, the *U*, *V*, and *W* Cagglioti parameters were fixed and corresponded to the instrumental broadening; hence, only the Lorentzian isotropic strain (*X*) and size (*Y*) parameters were refined. From these parameters, the isotropic apparent size and strain were calculated from Scherrer and Stokes-Wilson formula, respectively. Then, additional anisotropic size and strain parameters were also considered. Neutron diffraction investigation was useful for probing the structural features, since such a technique is less sensitive to preferred orientation phenomena. The NPD data were recorded in the D2B and D20 (for temperature-dependent patterns) diffractometers at the Institut Laue-Langevin in Grenoble (France). Neutron wavelengths of λ = 1.594 and 1.540 Å were used, respectively, for D2B in high resolution configuration and D20 with a takeoff angle of 90°. Almost 1.2 g of sample was contained in a cylindrical vanadium holder (6 mm in diameter).

X-ray Photoelectron Spectroscopy. For the XPS measurements, the sample in powder form was deposited on clean double-stick carbon tape, loaded in a vacuum load-lock chamber, and then transferred in the ultrahigh vacuum system. The XPS chamber has a base pressure of 10^{-10} mbar and is equipped with a hemispherical electron energy Analyzer (*SPECS* Phoibos 100 spectrometer) and an Al Kα (1486.29 eV) X-ray source. The angle between the hemispherical analyzer and the plane of the surface was kept at 60°. Wide survey spectrum was recorded using an energy step of 0.5 eV and a pass-energy of 40 eV, while specific core levels spectra (P 2p, O 1s, C 1s, and VB) were acquired using an energy step of 0.1 eV and a pass-energy of 20 eV. Data processing was performed with *CasaXPS*© software. The absolute binding energies of the photoelectron spectra were determined by referencing to the C 1s core level at 285 eV.[19] The contributions of the Al Kα satellite lines were subtracted.

Transmission Electron Microscopy. Scanning transmission electron microscopy (STEM) was done in a JEOL ARM 200 electron microscope operated at 200 kV and equipped with the aberration corrector enabling the spatial resolution of 0.8 Å.

Thermoelectric Characterization. A Linseis LFA 1000 instrument was used to measure the thermal diffusivity (α) of the sample over a temperature range of 300 < *T* < 800 K by the laser-flash technique. A thin graphite coating was applied to the surface of the pellet to maximize heat absorption and emissivity. The thermal conductivity (κ) is determined using $\kappa = \alpha C_p \rho$, where C_p is the specific heat and ρ is the sample density (here, ρ = 2.46 g cm^{-3}). Specific heat was calculated using the Dulong–Petit equation. High temperature measurements (300 up to 773 K) of the electrical resistivity were performed in the Van der Pauw geometry, while the Seebeck coefficient was measured in a homemade apparatus.[20,21]

RESULTS AND DISCUSSION

Structural Properties. The crystal structure of black phosphorus was solved for the first time in 1935 by Hultgren et al. and revised many times with different techniques.[6] This allotrope of phosphorus was reported in orthorhombic symmetry, space group *Cmca* (*N*° 64 or D_{2h}^{18}). In order to describe the crystal structure of our black phosphorus obtained under high-pressure and high temperature conditions, synchrotron and neutron diffraction studies were carried out at room temperature (RT), as shown in Figure 1. From the refined NPD data, the following lattice parameters were derived: *a* = 3.3159(1) Å, *b* = 10.4772(4) Å, and *c* = 4.3724(2) Å. The P atoms are located at 8*f* Wyckoff sites (0, *y*, *z*), forming a corrugated layer where each sp^3 P atom is covalently bonded to three other adjacent P atoms in a triangular pyramid coordination environment. Adjacent layers are bonded by weak van der Waals (vdW) interactions along *b* axis and are stuck with an ABAB stacking sequence. The distance between two layers is about 5 Å. The refinement showed that the orthorhombic model leads to a good fit of the neutron diffraction pattern, as shown in Figure 1b.

https://dx.doi.org/10.1021/acs.inorgchem.0c01573
Inorg. Chem. XXXX, XXX, XXX−XXX

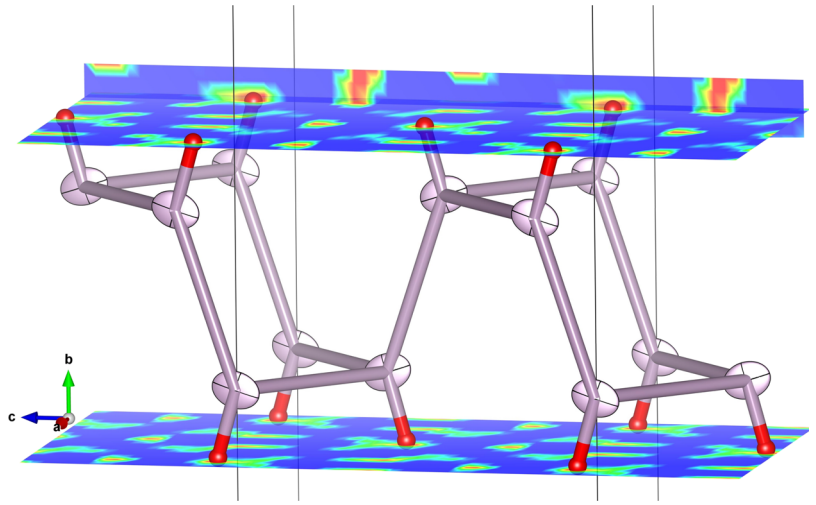

Figure 3. Lone pairs (red spheres) observed from X-N analysis. The planes parallel to (010) plane plots the Fourier difference maps between SXRD and NPD data.

The synchrotron pattern in Figure 1c was also well fitted using the orthorhombic model; however, some peaks showed a non-negligible mismatch, mainly in (021), (040), and (111) lines as shown in Figure 1d. A detailed inspection reveals that the mismatch is mainly due to differences in the peak broadening. The initial refinement with isotropic size and strain leads to the following results: 604 nm and 3.5×10^{-4} for crystallite size and strain, respectively. Nevertheless, the observed broadening evidenced the presence of anisotropic microstructural effects. Thus, several combinations of anisotropic models of size and/or strain were tested in order to improve the pattern matching. A good agreement was achieved considering the size as platelet and an anisotropic strain broadening in the *mmm* Laue class. Figure 1c illustrates the good agreement reached for SXRD pattern, and a detailed view of selected lines comparing the isotropic and anisotropic size/strain models is represented in Figure 1d. The shape results of these models are illustrated in Figure 2a,b. The platelet shape of the crystallite, perpendicular to the *b* axis, is not surprising in view of the layered nature of BP. The obtained strain shape seems to be harder to interpret in terms of crystal behavior. However, some features of the sample can be deduced. Figure 2c reveals that the major component of the strain is along (011) direction, but analysis of the individual strain of each plane shows that the main contributions are in the (0, 2*n*, *n*) plane family. A strain effect in this direction can be understood in terms of a short displacement of the sheets along the *c* axis, producing a smooth curvature in these planes. Figure 2c also schematizes the planes in which the strain effects are more significant. To our knowledge, these effects were never reported in literature so far. They were only detected due to a synergy of neutron and synchrotron X-ray diffraction techniques. From the NPD data, we obtained the atomic positions and lattice constants. From the SXRD, we derived the anisotropic strain effects by setting the mentioned parameters as fixed ones during the refinement.

The occurrence of strong strain effects is not so surprising, since the piston−cylinder press may lead to a nonhomogeneous pressure distribution within the sample. Some recent results on high-pressure stabilized La-filled skutterudite-type phases derived from $CoSb_3$ show that high-pressure synthesis followed by quenching is able to produce two coexisting La-filled skutterudite phases with uneven filling factor. It comes from a nonuniform pressure distribution, which dramatically reduced the thermal conductivity.[22] This result was perfectly reproduced for other filler elements, such as mischmetal,[23] cerium, and ytterbium,[24] in which low thermal conductivities were explained in light of the nanoscale mixing of two phases with distinct filling fractions. In the case of bulk BP, theoretical calculations have established that this compound is much harder along the *a* axis than along the *b* or *c* axes, as reflected in the Young's modulus along these axes:[25] 48.9, 15.7, and 15.1 GPa, respectively. In turn, it explains why strain effects occurred along (0, 2*n*, *n*) plane family in our bulk black phosphorus, since we have considered a nonuniform pressure distribution within the Nb capsule, leading to a strained crystal structure; see the model of Figure 2b (*mmm* Laue class).

The opportunity of combination of both synchrotron and neutron diffraction data may lead to the visualization of the phosphorus lone pair ($3s^2$) by comparing the electron and nuclear densities using the so-called X-N methods. In this procedure, the positions of the nuclei determined from neutron data were utilized to perform difference Fourier syntheses from SXRD data, which contain information on the electron distribution in the crystal. Then, difference Fourier maps (DFM) were used to find subtle electronic densities around P atom. By doing so, an electron density attributable to a lone electron pair was clearly unveiled. Figure 3 shows a layer of crystal structure with two sections of the DFM parallel to (010) plane, where the density assigned to the lone pair can be observed. The red spheres indicate the positions of maximum density, located at distances from the phosphorus atoms of 0.84 Å. This distance and position are in a good agreement with recent *ab initio* calculations, yielding P-lone pair distances of 0.85 Å.[26] Therefore, these experimental data allowed confirmation of theoretical analyses regarding the localization of the phosphorus $3s^2$ lone pair in BP.

STEM and Surface Chemistry. The scanning transmission electron microscopy images (STEM) show that the powder of BP obtained by grinding a high-pressure pellet consists of three-dimensional grains, rather than two-dimensional platelets, in panel a of Figure 4. The whole grain in panel a is oriented along the [110] zone axis, but some areas of the grain display some small (up to one degree) misalignments with respect to that axis. The crystalline structures obtained by high resolution annular

https://dx.doi.org/10.1021/acs.inorgchem.0c01573
Inorg. Chem. XXXX, XXX, XXX−XXX

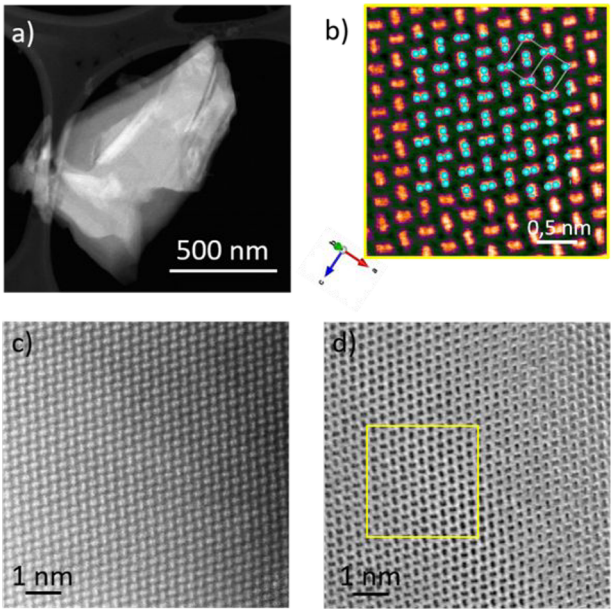

Figure 4. (a) STEM of three-dimensional grains of BP. (b) Artificially colored inverse ABF image. (c) High resolution annular dark field (ADF) and (d) annular bright field (ABF) imaging.

dark field (ADF) and annular bright field (ABF) imaging are represented in panels c and d, respectively. In both images (c and d), one can observe the pronounced defocusing (especially visible as blurred regions in the ABF image), which is the consequence of thickness differences at the edge of the grain. Atoms in ADF and ABF images appear as bright and dark spots, respectively. Figure 4b shows the artificially colored inverse ABF image (thus, the atoms are again bright spots) taken from the well-focused region in Figure 4d (yellow square). The dumbbells that appear in this crystal orientation and are visible in both panels c and d, are especially well resolved in panel b. The crystalline model based on the synchrotron data (cyan dots) fits perfectly to the microscopic image.

An XPS investigation was useful for probing the surface chemistry in bulk black phosphorus. Figure 5a exhibits the survey spectrum in which P, O, and C chemical elements appeared as expected. It is also interesting to notice the occurrence of energy loss peaks almost up to third order, which are satellites of the main P 2p and P 2s peaks.[27,28] They are related to the creation of plasmon excitations with E_p energy around 20.2 eV, which gives an electron density n of 2.96×10^{23} cm^{-3} by using the equation $n = m_e E_p^2/(4\pi e^2 \hbar^2)$.[29] The observed carbon signal located at 285 eV arises from adventitious carbon,[19] which was employed for calibration of the binding energy. High resolution XPS spectra at P 2p and O 1s core energies are depicted in panels b and c, respectively. The phosphorus P 2p photoelectron spectrum exhibits the spin−orbital splitting doublet located at 130.4 ($2p_{3/2}$) and 131.3 ($2p_{1/2}$) eV,[30] which are characteristic of crystalline black phosphorus. Phosphorus oxides could be detected as photoemission peaks in the range 132−136 eV. However, no such peaks were found in panel b. The oxygen O 1s photoelectron spectrum was decomposed into two components at binding energies of 531.8 and 533.6 eV, corresponding to OH surface groups and P−O−P groups of H_3PO_4 formed after a partial surface dehydrogenation, respectively.[31] In panel d, the photoelectron spectrum covering the valence electron (VB) interval exhibits five features concerning P 3p (3−7 eV) and P 3s (10−17 eV) orbitals.[32] It is also possible to estimate the valence band edge by applying a linear regression in the interval near 0 eV: the Fermi energy level (E_F). The obtained value was around 0.28 eV, confirming that our BP has a narrow semiconductor (p-type) character.

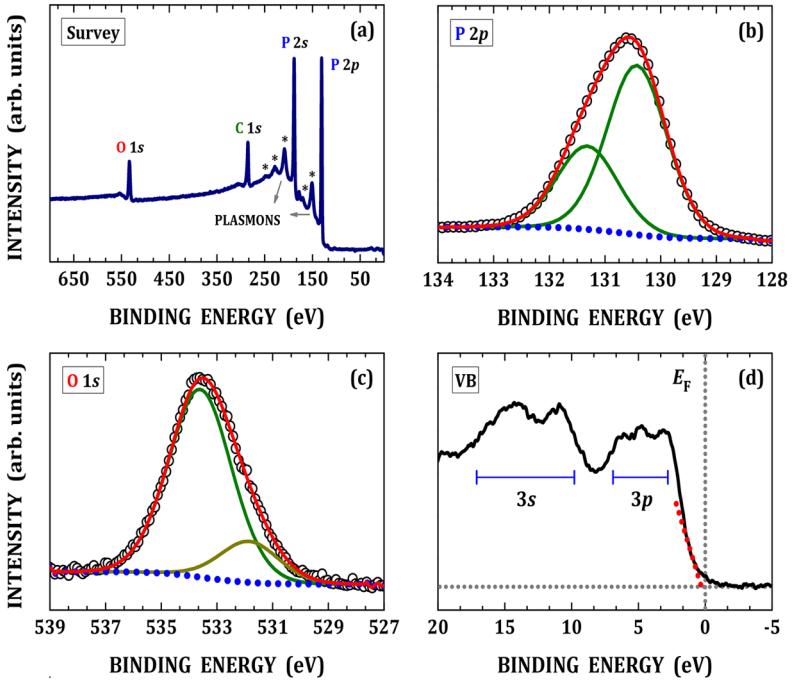

Figure 5. Photoelectron spectra of black phosphorus. (a) Survey scan, (b) P 2p, (c) O 1s, and (d) valence band region. In panels b and c, open circles and red lines are the experimental and fitted data. The Shirley-type background (dotted blue lines) was considered during the fitting process.

https://dx.doi.org/10.1021/acs.inorgchem.0c01573
Inorg. Chem. XXXX, XXX, XXX−XXX

Electrical Resistivity and Magnetoresistance. The resistivity measurements were performed on a bulk piece of BP in two alternative geometries: using the in-line four-probe method at low temperature and the Van der Pauw technique above room temperature, as shown in Figure 6a from 2 up to 780

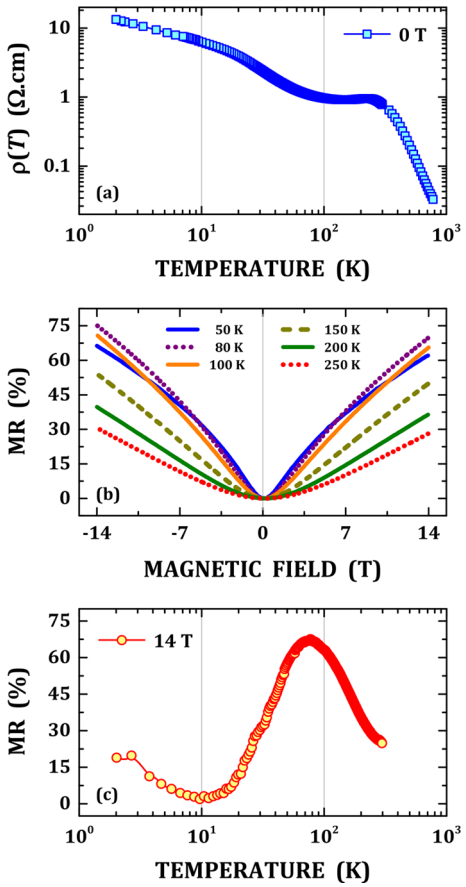

Figure 6. Electrical resistivity of BP taken for 0 T from 2 up to 780 K (a). Magnetoresistance curves as a function of the applied magnetic field for some selected temperatures (b). MR curve against temperature for 14 T (c).

K without applied magnetic field. The behavior of the resistivity $\rho(T)$ curve below room temperature, 2−300 K, is similar to earlier reports.[33,34] Above 225 K, the resistivity decreases as temperature increases due to thermally activated charge carriers, i.e., a typical semiconducting behavior. Below 20 K, the resistivity saturates, corresponding to a two-dimensional Anderson localization.[35] In the temperature range 20−225 K, the resistivity has a minimum at around 150 K. This resistivity anomaly was earlier assigned to a lattice vibration suppression, which induces an enhanced mobility;[34] however, this behavior is still an open question in the literature and we will try to explore it in this work.

From the temperature dependence of the resistivity in the intrinsic semiconducting regime, we can estimate the bandgap, E_g: $\rho(T) \propto \exp(E_g/2k_BT)$. From Figure 6a, the gap energy was evaluated in two temperature ranges, 340−450 and 460−780 K, giving energies of 0.2 and 0.4 eV, respectively. It means that two conduction mechanisms play a role at high temperatures in BP. This can be compared to the XPS results. From the XPS spectrum in Figure 5d, the valence band edge energy of black phosphorus was estimated by linear extrapolation from bands to the baseline, yielding 0.28 eV relative to the Fermi level, in good agreement with reported E_g for bulk BP.[2,3,15,33] This bandgap is comparable to those reported for layered thermoelectric materials with narrow bandgap, such as Bi_2Te_3 with E_g around 0.1−0.15 eV.[36]

Anisotropic linear magnetoresistance in single crystalline BP was already reported previously.[37] MR can be as large as 510% in fields of 7 T, with current in the *ac* plane and magnetic field applied parallel to the *b* axis (through plane) of the orthorhombic lattice of BP. Here, the magnetoresistance is understood as $MR(\%) = 100 \times [\rho(B) - \rho(0)]/\rho(0)$, where B is the applied magnetic field. This is despite the fact that BP is nonmagnetic. However, this behavior is relatively new and has attracted attention due to the extremely large magnetoresistance (X-MR) observed in semimetals, including NbP,[38] TaAs,[39] Cd_3As_2,[40] WTe_2.[41]

In order to verify the MR phenomenon in our BP sample, we performed a series of resistivity measurements using the same in-line four-probe geometry as a function of applied magnetic field and temperature. Figure 6b summarized the dependence of magnetoresistance with magnetic field for some selected temperatures. For almost all of them, a linear behavior is observed above a threshold field of B_L not exhibiting a saturation sign. At 50 K, the $MR(\%) \times B$ curve seems to be nonlinear in the entire magnetic field range from −14 up to 14 T. Panel c of Figure 6 exhibits the temperature dependence of magnetoresistance for 14 T of applied magnetic field. A typical maximum in the curve is noticed at 78 K with 67% in MR(%); then it vanishes around 10 K and starts to increase again at low temperature. The maximum MR for this HP synthesized polycrystalline BP is considerably lower than that reported for single crystals.[17,37] In order to address the minimum in the electrical resistivity near 150 K for 0 T in BP, we performed neutron diffraction experiments in the temperature interval 20−250 K, as discussed in the following section. A main question at this point: Is there any anomaly concerning the structural parameters, which can be correlated to the minimum in $\rho(T)$?

Temperature-Dependent Neutron Diffraction. The BP exhibits a pressure-induced band-overlapped metallization around 1.38−1.5 GPa.[33,34] Such results were exhaustively confirmed by different techniques, including resistivity measurements and optical and infrared reflectivity spectroscopies under high hydrostatic pressure. The metallization process in BP is still under debate, and some hypotheses were raised in terms of a strong electron−phonon interaction[42] or an excitonic phase as explained by Mott.[43] Akiba et al. recently showed that the semiconducting behavior in BP can be explained by a two-carrier model, with different densities and mobilities, for pressures below 0.29 GPa.[34] This model is unsatisfactory for explaining the large magnetoresistance observed in the semimetallic state under pressure (above 1.43 GPa). Superconducting states of BP under magnetic field and high-pressure was also reported.[44]

For further insights into the anomalous behavior in electrical resistivity around 150 K, as also reported in literature,[17,34,45] we have recorded sequential neutron diffraction patterns ranging from 20 to 250 K (for the cooling regime). Some refined patterns are displayed in details in Figure 7 at selected temperatures. The thermal evolution of the structural parameters across the anomalous range in black phosphorus can be seen in Figure 8. An unreported result occurred for the *a* unit-cell parameter (zigzag) and its dependence with temperature, and indeed, a *quasi*-temperature-independent thermal expansion can be noticed in the temperature range 20−150 K in

https://dx.doi.org/10.1021/acs.inorgchem.0c01573
Inorg. Chem. XXXX, XXX, XXX−XXX

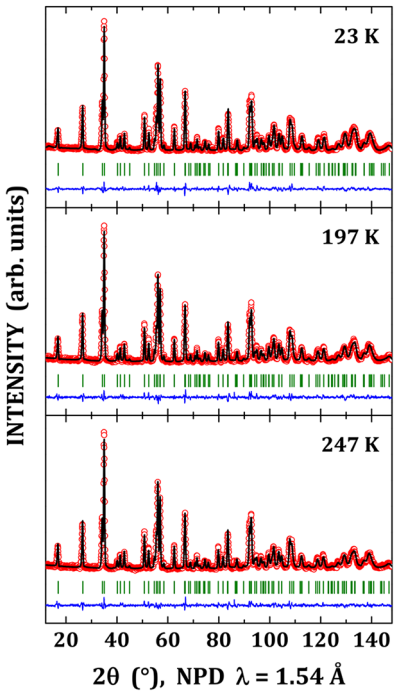

Figure 7. Selected Rietveld refined neutron diffraction patterns collected at 23, 197, and 247 K. Red open circles represent the experimental data, black lines refer to calculated profile, blue lines are the difference pattern between experimental and calculated data, and dark green bars denote the Bragg reflections.

panel a of Figure 8. This result was corroborated in a second run acquisition during the warming regime with a better temperature resolution. Also, an anomaly is visible in this temperature range for the *b* and *c* unit-cell parameters in panels b and c, respectively. Evidently, these trends are reflected in the unit-cell volume dependence with temperature, as shown in Figure 8f; however, they do not show a *quasi*-temperature-independence in the thermal expansion but only a slight cusp near 150 K. The thermal parameters including the anisotropic thermal displacements β_{22} and β_{33} did not depict any special anomalies in this temperature interval. They can be analyzed in terms of a Debye-model[22,24] to estimate the Debye-temperature as 491.5 K with a relatively large disorder parameter of 0.06 Å.

A recent theoretical work on the black phosphorene showed that a negative thermal expansion (NTE) can occur for temperatures below 200 K[46] in which a negative coefficient of thermal expansion (CTE) may reach a value of −7.4 ppm K^{-1}. The authors predicted a volume-NTE behavior with a high anisotropy in in-plane thermal trend for both zigzag (*a* axis) and armchair directions (*c* axis). Slight variations were also seen in the two characteristic angles θ_{213} and θ_{145} in the temperature range 100−200 K. Such angles describe the hinge-like structure of phosphorene in such a way that the former concerns the zigzag direction, while the latter relates to the armchair one (see the sketch in Figure 2d). The negative thermal expansion has become an important feature of materials properties, as represented by the progressive increase of works on such a theme. It can be mentioned the case of ScF_3,[47] NpFeAsO,[48] $(Al_{0.2}Zr_{0.8})_{20/19}Nb(PO_4)_3$,[49] and $Gd_5(Si,Ge)_4$.[50]

A local structure analysis was performed based on the distances (d_1 and d_2) and angles (θ_{213} and θ_{145}) and their dependence with temperature. A sketch of a small local unit showing BP angles and distances is represented in Figure 2d. The thermal dependences of d_1, d_2, θ_{213}, and θ_{145} parameters are displayed in Figure 9. A trend can be distinguished in d_2 distance: it shows a slight decrease in the temperature range 70−200 K, reaching a minimum at 125 K. The error in bond distance or angle carries the error of atomic fractional position, lattice parameters, and the thermal displacement. It may explain the relatively large error bars in Figure 9. However, it is difficult to conclude whether a negative thermal expansion (NTE) takes place in our BP; it is more convincing to say that the zigzag direction (*a* axis) has a *quasi*-temperature-independent behavior in the range 20−150 K.

According to the local structure representation, we see that a hypothetical reduction in the d_2 bond-distance increases the overlap of the P electronic densities, which in turn further reduces the bandgap and may lead an increased electronic conductivity. Then, based on the temperature-dependent NPD data, which unveil the anisotropic nature of the lattice thermal expansion, we are able to correlate the minimum in the electrical resistivity of BP around 150 K with the anomalous temperature-independent thermal expansion through the *a* unit-cell direction (zigzag). This behavior, at least, may enhance the electronic density in this temperature regime and then affect the electrical resistivity. Although the NPD patterns were collected without magnetic field, the temperature-independent thermal expansion could be a key to understand the anomalous magnetoresistance in BP. However, further structural studies in the presence of an applied magnetic field would be essential to precisely address the magnetoresistance phenomenon.

Thermoelectric Properties. Regarding the literature of thermoelectric features in BP, anisotropic transport in single crystalline samples was reported.[15,51] Recent papers[17,51] have revisited the classical results on thermoelectric data using modern material characterization techniques. For instance, Zeng et al. studied the anisotropic behavior of the thermoelectric properties in high quality BP crystals obtained by chemical vapor transport method.[15]

In Figure 10a, we present the high temperature thermoelectric properties of high-pressure synthesized polycrystalline BP, between 300 and 723 K. The electrical conductivity (Figure 10a) is around 1.5 S cm^{-1} at RT, below values found for single crystal BP. This is expected, considering a resistive blocking effect due to the grain boundary formation in polycrystalline samples.[52] The Seebeck coefficient in Figure 10b is positive in the entire temperature range, corresponding to the *p*-type carriers. In previous reports on the BP single-crystal, the temperature-dependent Seebeck coefficient depicts a maximum value (S_{max}) at a critical temperature T_{max}, allowing estimation of the bandgap: $S_{max}T_{max} = E_g/2e$, where *e* is the electron charge.[53] Typical values in BP for S_{max} are 415−452 μVK^{-1} with T_{max} of 380−425 K, leading to E_g values of 0.32−0.38 eV.[15,51] However, for our polycrystalline BP, the Seebeck coefficient is smaller and it decreases almost linearly with temperature, displaying only a *quasi*-anomalous effect at 400−425 K, a slight bump. It can be interpreted as an additional charge carrier mechanism above 400 K, as also implied by the temperature-dependent resistivity in Figure 6a, which hinders the analysis of the bandgap from the maximum value of the Seebeck coefficient. The power factor ($PF = S^2\sigma$) is drawn in Figure 10c for the temperature interval 300−723 K. At 323 K, the PF value was 10.6 $\mu Wm^{-1}K^{-2}$.

For thermoelectricity, many efforts have been devoted to reducing the lattice contribution to the thermal conductivity. Our high-pressure synthesized BP succeeds remarkably well in

https://dx.doi.org/10.1021/acs.inorgchem.0c01573
Inorg. Chem. XXXX, XXX, XXX−XXX

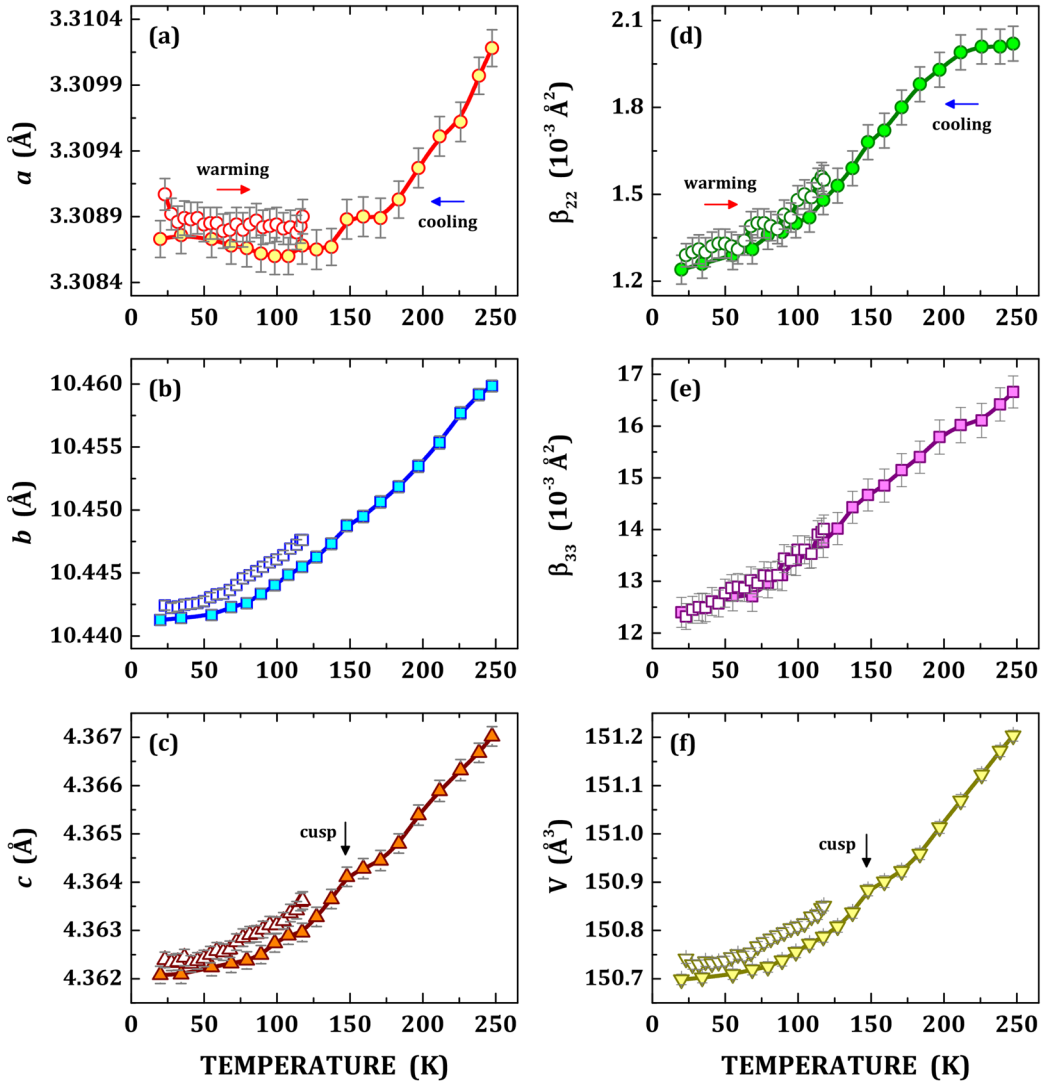

Figure 8. Thermal dependence of the refined parameters of BP from NPD data, including the lattice constants (a (a), b (b), c (c), and V (f)) and the anisotropic thermal displacement components (β_{22} (d) and β_{33} (e)). Filled symbols represent the acquisition under cooling, while the open symbols represent the data under warming.

this regard (Figure 10d). In the entire temperature range above room temperature, the thermal conductivity is governed by the Umklapp process for the phonon scattering, since the reciprocal of temperature-type behavior (T^{-1}) is respected. One can observe that κ_T varies from 14.5 to 6.2 $Wm^{-1}K^{-1}$ in the range 323−673 K, which is remarkably below the values reported for single-crystal measurements along the three axes.[15] The Wiedemann−Franz law, $\kappa_{ele} = L\sigma T$, was taken into account to separate the electronic and lattice contributions from the total thermal conductivity (Figure 10e). Because of the relatively high resistivity of the bulk BP, the total thermal conductivity reflects almost its lattice contribution (κ_{lat}). The electronic part of the thermal conductivity reached only 0.02 $Wm^{-1}K^{-1}$ at 673 K. Note that the last point for κ_T at 723 K may represents the onset of the transition from black to red phosphorus, and measurements above this temperature were disregarded here.

The thermoelectric Figure of Merit, $zT = S^2\sigma T/\kappa_T$, for our HP-synthesized BP is shown in Figure 10f, which reaches a maximum value of 5.6×10^{-3} at 723 K. It is limited by the high resistivity and somewhat reduced Seebeck coefficient despite the improved (reduced) thermal conductivity. We can treat this Figure of Merit as a function of two independent variables: the quality factor B and the reduced chemical potential η.[54] The quality factor parameter can be used to evaluate the optimal zT value in thermoelectric materials, since it is a property largely independent of doping. The B parameter expression is shown in eq 1

$$B = \left(\frac{k_B}{e}\right)^2 \frac{\sigma_{E_0}}{\kappa_L} T \quad (1)$$

where k_B is the Boltzmann's constant, e is the elementary charge, σ_{E0} is a transport coefficient with units of conductivity, k_L is the lattice thermal conductivity, and T is the absolute temperature. The calculation of this quality factor is displayed in Figure 11a. It shows a linear dependence between 450 and 650 K, reaching its highest value of 1.85×10^{-3} at 723 K, just before the presumed black-to-red transition.

Unlike the quality factor, the reduced chemical potential is a function of both chemical doping and temperature, and we can extract it from the Seebeck coefficient. This η indicates the doping level, which depends on defects and impurities, and in order to optimize the zT, this η must be tuned to an optimal

https://dx.doi.org/10.1021/acs.inorgchem.0c01573
Inorg. Chem. XXXX, XXX, XXX−XXX

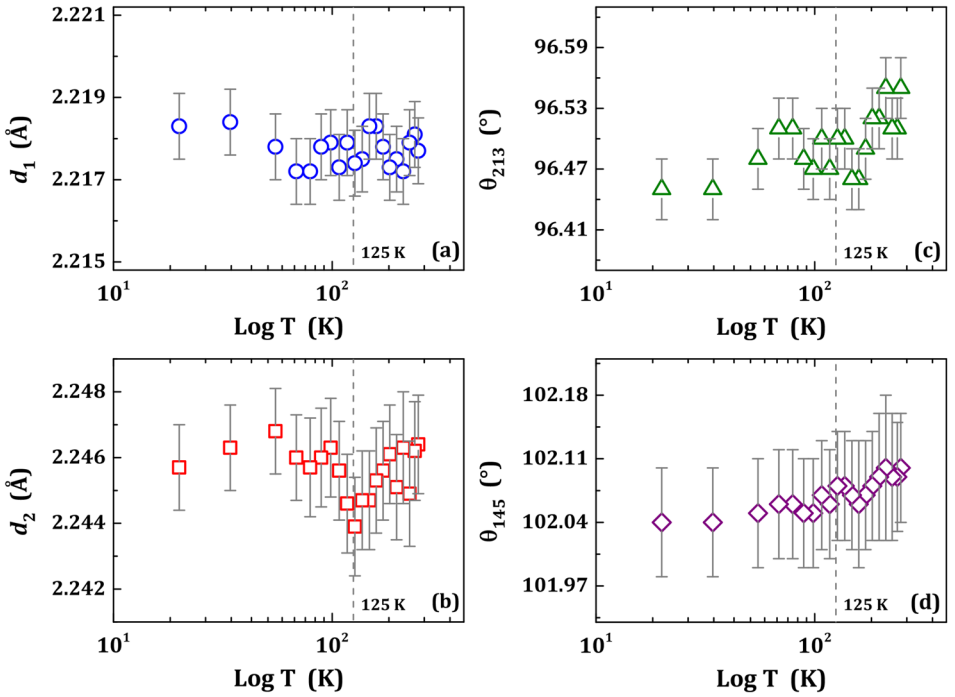

Figure 9. Local structure analysis of BP as a function of temperature (in log scale). The bonds d_1 (a) and d_2 (b), as well as the bond-angles θ_{213} (c) and θ_{145} (d) are defined in panel d of Figure 2.

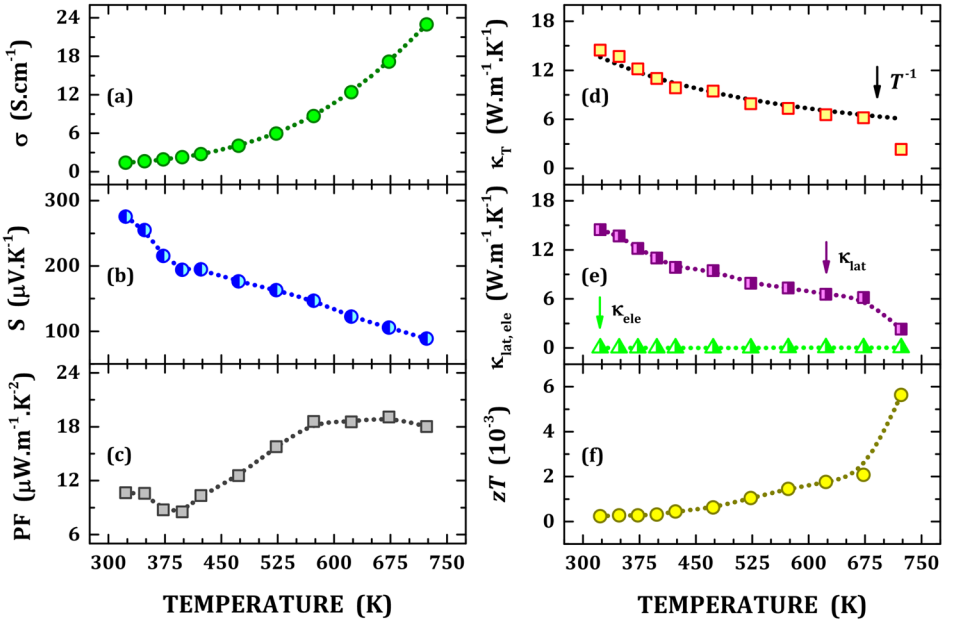

Figure 10. Temperature dependence of electric conductivity (a), Seebeck coefficient (b), power factor (PF) (c), total thermal conductivity (d) and its electronic and lattice components (e), and Figure of Merit zT (f) of BP sample synthesized by high-pressure procedure.

value via doping. The zT vs η curves for four selected temperatures are shown in Figure 11b. The maximum achievable Figure of Merit increases as temperatures increases, with a highest value of 7.5×10^{-3} at 723 K. The experimentally measured zT is comparable to these predicted data, and considering that the reduced chemical potential can be tuned by an adequate doping, this black phosphorus could still achieve a better thermoelectric performance, although it would still be far from competitive values.

CONCLUSIONS

We have successfully synthesized large bulk black phosphorus pieces under high-pressure and high temperature conditions. Due to the nonuniform pressure distribution within the Nb capsule during the synthesis, our BP exhibited an anisotropic strained lattice as described by the *mmm* Laue class. The joint analyses of SXRD and NDP data at room temperature yield crystallographic evidence on the location of the phosphorus lone pair $3s^2$, as predicted from *ab initio* calculations. Neutron diffraction as a function of temperature revealed a *quasi-*

https://dx.doi.org/10.1021/acs.inorgchem.0c01573
Inorg. Chem. XXXX, XXX, XXX−XXX

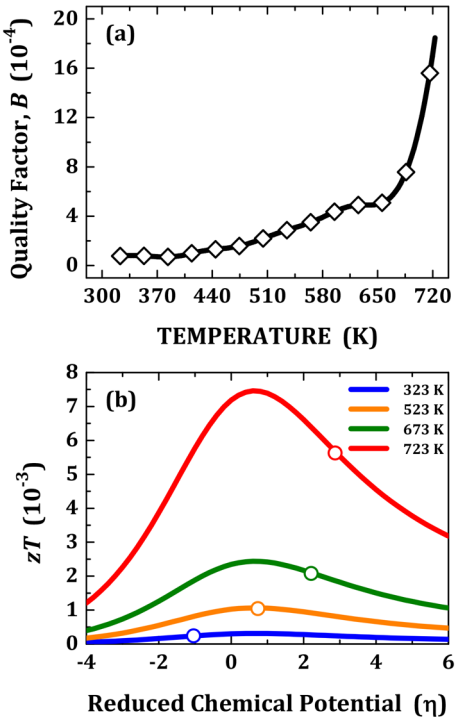

Figure 11. Quality factor B of black phosphorus synthesized by high-pressure method as a function of temperature (a). zT *vs* reduced chemical potential (η) curves predicted by the quality factor at several temperatures, shown together with the points experimentally measured in the sample. This zT could be optimized modifying the chemical potential by an adequate doping (b).

temperature-independent thermal expansion, which was correlated with the anomalous electrical behavior at low temperature, already known for the bulk black phosphorus. A better overlap of the phosphorus electronic density is derived from the shortening of the *a* axis upon heating, which accounts for a minimum in the electrical resistivity of BP at 150 K. Thermoelectric properties at high temperature were also studied in our polycrystalline BP, which exhibited a variation of the thermal conductivity from 14.5 to 6.2 $Wm^{-1}K^{-1}$ in the range 323−673 K, i.e., below the values already reported for single-crystals.

■ ASSOCIATED CONTENT

Supporting Information

The Supporting Information is available free of charge at https://pubs.acs.org/doi/10.1021/acs.inorgchem.0c01573.

Fitting of the lattice thermal conductivity (κ_L) using the Callaway model, more details on the quality factor analysis (PDF)

■ AUTHOR INFORMATION

Corresponding Authors

João Elias F. S. Rodrigues − *Instituto de Ciencia de Materiales de Madrid, E-28049 Madrid, Spain;* orcid.org/0000-0002-9220-5809; Email: joaoelias.rodrigues@csic.es, rodrigues.joaoelias@gmail.com

José Antonio Alonso − *Instituto de Ciencia de Materiales de Madrid, E-28049 Madrid, Spain;* orcid.org/0000-0001-5329-1225; Email: ja.alonso@icmm.csic.es

Authors

Javier Gainza − *Instituto de Ciencia de Materiales de Madrid, E-28049 Madrid, Spain*

Federico Serrano-Sánchez − *Instituto de Ciencia de Materiales de Madrid, E-28049 Madrid, Spain*

Carlos López − *INTEQUI, (UNSL-CONICET), and Fac. de Química, Bioquímica y Farmacia, UNSL, 5700 San Luis, Argentina*

Oscar J. Dura − *Departamento de Física Aplicada, Universidad de Castilla-La Mancha, E-13071 Ciudad Real, Spain*

Norbert Nemes − *Instituto de Ciencia de Materiales de Madrid, E-28049 Madrid, Spain; Departamento de Fisica de Materiales, Universidad Complutense de Madrid, E-28040 Madrid, Spain*

Jose L. Martinez − *Instituto de Ciencia de Materiales de Madrid, E-28049 Madrid, Spain*

Yves Huttel − *Instituto de Ciencia de Materiales de Madrid, E-28049 Madrid, Spain*

Francois Fauth − *CELLS−ALBA Synchrotron, E-08290 Barcelona, Spain;* orcid.org/0000-0001-9465-3106

Maria Teresa Fernández-Diaz − *Institut Laue Langevin, F-38042 Grenoble, France*

Nevenko Biškup − *Departamento de Física de Materiales and Instituto Pluridisciplinar, Universidad Complutense de Madrid, E-28040 Madrid, Spain*

Complete contact information is available at: https://pubs.acs.org/10.1021/acs.inorgchem.0c01573

Author Contributions

J.E.R. and J.A.A. carried out the synthesis of the samples, structural characterization using laboratory XRD, NPD, and SXRD, and further discussion on the transport data. J.G. and F.S.S performed the Seebeck characterization and further discussion. C.A.L carried out the strain and lone electron pair analyses. O.J.D. conducted the thermoelectric characterization above room temperature. J.L.M and N.M.N performed the low temperature MR studies. J.E.R and Y.H. conducted the XPS studies and further discussion. F.F. provided the synchrotron facility. M.T.F-D provided the neutron facility. N.B. carried out the STEM analyses. J.A.A and J.L.M conceived the project. All of the authors participated in writing the manuscript and discussion of the results.

Notes

The authors declare no competing financial interest.

■ ACKNOWLEDGMENTS

The Spanish authors thank the Spanish Ministry of Science, Innovation, and Universities for funding the project MAT2017-84496-R, and RTI2018-097895-B-C43. J.E.R. is grateful to the Brazilian agency CAPES due to the fellowship (Finance Code 001:88881.171031/2018-01). J.G. thanks MICINN for granting the contract PRE2018-083398. CAL acknowledges ANPCyT and UNSL for financial support (projects PICT 2017-1842 and PROICO 2-2016). The crystalline models were done using *VESTA* software. The authors wish to express their gratitude to CELLS-ALBA technical staff for making the facilities available for the synchrotron X-ray powder diffraction experiment, and to ILL for making all facilities available for the neutron diffraction experiments.

■ REFERENCES

(1) Castellanos-Gomez, A. Black Phosphorus: Narrow Gap, Wide Applications. *J. Phys. Chem. Lett.* **2015**, *6* (21), 4280−4291.

https://dx.doi.org/10.1021/acs.inorgchem.0c01573
Inorg. Chem. XXXX, XXX, XXX−XXX

(2) Carvalho, A.; Wang, M.; Zhu, X.; Rodin, A. S.; Su, H.; Castro Neto, A. H. Phosphorene: From Theory to Applications. *Nat. Rev. Mater.* **2016**, *1* (11), 16061.
(3) Das, S.; Zhang, W.; Demarteau, M.; Hoffmann, A.; Dubey, M.; Roelofs, A. Tunable Transport Gap in Phosphorene. *Nano Lett.* **2014**, *14* (10), 5733−5739.
(4) Qiao, J.; Kong, X.; Hu, Z. X.; Yang, F.; Ji, W. High-Mobility Transport Anisotropy and Linear Dichroism in Few-Layer Black Phosphorus. *Nat. Commun.* **2014**, *5*, 1−7.
(5) Takao, Y.; Asahina, H.; Morita, A. Electronic Structure of Black Phosphorus in Tight Binding Approach. *J. Phys. Soc. Jpn.* **1981**, *50* (10), 3362−3369.
(6) Hultgren, R.; Gingrich, N. S.; Warren, B. E. The Atomic Distribution in Red and Black Phosphorus and the Crystal Structure of Black Phosphorus. *J. Chem. Phys.* **1935**, *3* (6), 351−355.
(7) Zhou, F.; Ouyang, L.; Zeng, M.; Liu, J.; Wang, H.; Shao, H.; Zhu, M. Growth Mechanism of Black Phosphorus Synthesized by Different Ball Milling Techniques. *J. Alloys Compd.* **2019**, *784*, 339−346.
(8) Köpf, M.; Eckstein, N.; Pfister, D.; Grotz, C.; Krüger, I.; Greiwe, M.; Hansen, T.; Kohlmann, H.; Nilges, T. Access and in Situ Growth of Phosphorene-Precursor Black Phosphorus. *J. Cryst. Growth* **2014**, *405*, 6−10.
(9) Shirotani, I. Growth of Large Single Crystals of Black Phosphorus at High Pressures and Temperatures, and Its Electrical Properties. *Mol. Cryst. Liq. Cryst.* **1982**, *86* (1), 203−211.
(10) Sun, Q.; Zhao, X.; Feng, Y.; Wu, Y.; Zhang, Z.; Zhang, X.; Wang, X.; Feng, S.; Liu, X. Pressure Quenching: A New Route for the Synthesis of Black Phosphorus. *Inorg. Chem. Front.* **2018**, *5* (3), 669−674.
(11) Bridgman, P. W. Two New Modifications of Phosphorus. *J. Am. Chem. Soc.* **1914**, *36* (7), 1344−1363.
(12) Bridgman, P. W. Further Note on Black Phosphorus. *J. Am. Chem. Soc.* **1916**, *38* (3), 609−612.
(13) Suryanarayana, C. Mechanical Alloying and Milling. *Prog. Mater. Sci.* **2001**, *46* (1−2), 1−184.
(14) Flores, E.; Ares, J. R.; Castellanos-Gomez, A.; Barawi, M.; Ferrer, I. J.; Sánchez, C. Thermoelectric Power of Bulk Black-Phosphorus. *Appl. Phys. Lett.* **2015**, *106* (2), 12−16.
(15) Zeng, Q.; Sun, B.; Du, K.; Zhao, W.; Yu, P.; Zhu, C.; Xia, J.; Chen, Y.; Cao, X.; Yan, Q.; Shen, Z.; Yu, T.; Long, Y.; Koh, Y. K.; Liu, Z. Highly Anisotropic Thermoelectric Properties of Black Phosphorus Crystals. *2D Mater.* **2019**, *6* (4), No. 045009.
(16) Zhang, J.; Liu, H. J.; Cheng, L.; Wei, J.; Liang, J. H.; Fan, D. D.; Jiang, P. H.; Sun, L.; Shi, J. High Thermoelectric Performance Can Be Achieved in Black Phosphorus. *J. Mater. Chem. C* **2016**, *4* (5), 991−998.
(17) Hu, S.; Xiang, J.; Lv, M.; Zhang, J.; Zhao, H.; Li, C.; Chen, G.; Wang, W.; Sun, P. Intrinsic and Extrinsic Electrical and Thermal Transport of Bulk Black Phosphorus. *Phys. Rev. B: Condens. Matter Mater. Phys.* **2018**, *97* (4), 1−8.
(18) Rodríguez-Carvajal, J. Recent Advances in Magnetic Structure Determination by Neutron Powder Diffraction. *Phys. B* **1993**, *192* (1−2), 55−69.
(19) Nevshupa, R.; Martínez, L.; Álvarez, L.; López, M. F.; Huttel, Y.; Méndez, J.; Román, E. Influence of Thermal Ageing on Surface Degradation of Ethylene-Propylene-Diene Elastomer. *J. Appl. Polym. Sci.* **2011**, *119* (1), 242−251.
(20) Iwanaga, S.; Toberer, E. S.; LaLonde, A.; Snyder, G. J. A. High Temperature Apparatus for Measurement of the Seebeck Coefficient. *Rev. Sci. Instrum.* **2011**, *82* (6), No. 063905.
(21) Gainza, J.; Serrano-Sánchez, F.; Gharsallah, M.; Funes, M.; Carrascoso, F.; Nemes, N. M.; Dura, O. J.; Martínez, J. L.; Alonso, J. A. Nanostructured Thermoelectric Chalcogenides. In *Bringing Thermoelectricity into Reality*; 2018; pp 3−22. DOI: 10.5772/intechopen.75442.
(22) Serrano-Sánchez, F.; Prado-Gonjal, J.; Nemes, N. M.; Biskup, N.; Varela, M.; Dura, O. J.; Martínez, J. L.; Fernández-Díaz, M. T.; Fauth, F.; Alonso, J. A. Low Thermal Conductivity in La-Filled Cobalt Antimonide Skutterudites with an Inhomogeneous Filling Factor Prepared under High-Pressure Conditions. *J. Mater. Chem. A* **2018**, *6* (1), 118−126.
(23) Gainza, J.; Serrano-Sánchez, F.; Prado-Gonjal, J.; Nemes, N.; Biskup, N.; Durá, O. J.; Martinez, J. L.; Fauth, F.; Alonso, J. A. Substantial Thermal Conductivity Reduction in Mischmetal Skutterudites $Mm_xCo_4Sb_{12}$ Prepared under High-Pressure Conditions, Due to Uneven Distribution of the Rare-Earth Elements. *J. Mater. Chem. C* **2019**, *7*, 4124−4131.
(24) Serrano-Sánchez, F.; Prado-Gonjal, J.; Nemes, N. M.; Biskup, N.; Dura, O. J.; Martínez, J. L.; Fernández-Díaz, M. T.; Fauth, F.; Alonso, J. A. Thermal Conductivity Reduction by Fluctuation of the Filling Fraction in Filled Cobalt Antimonide Skutterudite Thermoelectrics. *ACS Appl. Energy Mater.* **2018**, *1* (11), 6181−6189.
(25) Qin, G.; Yan, Q.-B.; Qin, Z.; Yue, S.-Y.; Cui, H.-J.; Zheng, Q.-R.; Su, G. Hinge-like Structure Induced Unusual Properties of Black Phosphorus and New Strategies to Improve the Thermoelectric Performance. *Sci. Rep.* **2014**, *4* (1), 6946.
(26) Galy, J.; Vignoles, G. L. The Role of P $3s^2$ Lone Pair (E) in Structure, Properties and Phase Transitions of Black Phosphorus. Stereochemistry and Ab Initio Topology Analyses. *Solid State Sci.* **2020**, *100*, 106068.
(27) Harada, Y.; Murano, K.; Shirotani, I.; Takahashi, T.; Maruyama, Y. Electronic Structure of Black Phosphorus Studied by X-Ray Photoelectron Spectroscopy. *Solid State Commun.* **1982**, *44* (6), 877−879.
(28) David, D. G. F.; Godet, C.; Johansson, F. O. L.; Lindblad, A. Quantitative Analysis of Plasmon Excitations in Hard X-Ray Photoelectron Spectra of Bulk Black Phosphorus. *Appl. Surf. Sci.* **2020**, *505*, 144385.
(29) Knox, R. S. *Solid State Physics, Suppl. 5: Theory of Excitons*; Solid state physics: advances in research and applications; Academic Press: New York, 1963.
(30) Moffat, T. P.; Latanision, R. M.; Ruf, R. R. An X-Ray Photoelectron Spectroscopy Study of Chromium-Metalloid Alloys-III. *Electrochim. Acta* **1995**, *40* (11), 1723−1734.
(31) Luo, W.; Zemlyanov, D. Y.; Milligan, C. A.; Du, Y.; Yang, L.; Wu, Y.; Ye, P. D. Surface Chemistry of Black Phosphorus under a Controlled Oxidative Environment. *Nanotechnology* **2016**, *27* (43), 434002.
(32) Asahina, H.; Morita, A. Band Structure and Optical Properties of Black Phosphorus. *J. Phys. C: Solid State Phys.* **1984**, *17* (11), 1839−1852.
(33) Akahama, Y.; Kawamura, H. Optical and Electrical Studies on Band-Overlapped Metallization of the Narrow-Gap Semiconductor Black Phosphorus with Layered Structure. *Phys. Status Solidi B* **2001**, *223* (1), 349−353.
(34) Akiba, K.; Miyake, A.; Akahama, Y.; Matsubayashi, K.; Uwatoko, Y.; Tokunaga, M. Two-Carrier Analyses of the Transport Properties of Black Phosphorus under Pressure. *Phys. Rev. B: Condens. Matter Mater. Phys.* **2017**, *95* (11), 1−7.
(35) Baba, M.; Izumida, F.; Takeda, Y.; Shibata, K.; Morita, A.; Koike, Y.; Fukase, T. Two-Dimensional Anderson Localization in Black Phosphorus Crystals Prepared by Bismuth-Flux Method. *J. Phys. Soc. Jpn.* **1991**, *60*, 3777−3783.
(36) Greenaway, D. L.; Harbeke, G. Band Structure of Bismuth Telluride, Bismuth Selenide and Their Respective Alloys. *J. Phys. Chem. Solids* **1965**, *26* (10), 1585−1604.
(37) Hou, Z.; Yang, B.; Wang, Y.; Ding, B.; Zhang, X.; Yao, Y.; Liu, E.; Xi, X.; Wu, G.; Zeng, Z.; Liu, Z.; Wang, W. Large and Anisotropic Linear Magnetoresistance in Single Crystals of Black Phosphorus Arising from Mobility Fluctuations. *Sci. Rep.* **2016**, *6* (March), 1−7.
(38) Shekhar, C.; Nayak, A. K.; Sun, Y.; Schmidt, M.; Nicklas, M.; Leermakers, I.; Zeitler, U.; Skourski, Y.; Wosnitza, J.; Liu, Z.; Chen, Y.; Schnelle, W.; Borrmann, H.; Grin, Y.; Felser, C.; Yan, B. Extremely Large Magnetoresistance and Ultrahigh Mobility in the Topological Weyl Semimetal Candidate NbP. *Nat. Phys.* **2015**, *11* (8), 645−649.
(39) Huang, X.; Zhao, L.; Long, Y.; Wang, P.; Chen, D.; Yang, Z.; Liang, H.; Xue, M.; Weng, H.; Fang, Z.; Dai, X.; Chen, G. Observation of the Chiral-Anomaly-Induced Negative Magnetoresistance: In 3D Weyl Semimetal TaAs. *Phys. Rev. X* **2015**, *5* (3), 1−9.

https://dx.doi.org/10.1021/acs.inorgchem.0c01573
Inorg. Chem. XXXX, XXX, XXX−XXX

(40) Liang, T.; Gibson, Q.; Ali, M. N.; Liu, M.; Cava, R. J.; Ong, N. P. Ultrahigh Mobility and Giant Magnetoresistance in the Dirac Semimetal Cd_3As_2. *Nat. Mater.* **2015**, *14* (3), 280−284.
(41) Ali, M. N.; Xiong, J.; Flynn, S.; Tao, J.; Gibson, Q. D.; Schoop, L. M.; Liang, T.; Haldolaarachchige, N.; Hirschberger, M.; Ong, N. P.; Cava, R. J. Large, Non-Saturating Magnetoresistance in WTe_2. *Nature* **2014**, *514* (7521), 205−208.
(42) Aoki, M.; Suzuki, N. Electron-Lattice Interaction and Lattice Dynamics in Black Phosphorus. *J. Phys. Soc. Jpn.* **1987**, *56* (7), 2433−2447.
(43) Mott, N. F. The Transition to the Metallic State. *Philos. Mag.* **1961**, *6* (62), 287−309.
(44) Li, X.; Sun, J.; Shahi, P.; Gao, M.; MacDonald, A. H.; Uwatoko, Y.; Xiang, T.; Goodenough, J. B.; Cheng, J.; Zhou, J. Pressure-Induced Phase Transitions and Superconductivity in a Black Phosphorus Single Crystal. *Proc. Natl. Acad. Sci. U. S. A.* **2018**, *115* (40), 9935−9940.
(45) Akiba, K.; Miyake, A.; Yuichi, A.; Matsubayashi, K.; Uwatoko, Y.; Arai, H.; Fuseya, Y.; Tokunaga, M. Anomalous Quantum Transport Properties in Semimetallic Black Phosphorus. *J. Phys. Soc. Jpn.* **2015**, *84* (7), 2−5.
(46) Wang, L.; Wang, C.; Chen, Y. Black Phosphorene Exhibiting Negative Thermal Expansion and Negative Linear Compressibility. *J. Phys.: Condens. Matter* **2019**, *31* (46), 465003.
(47) Evans, H. A.; Wu, Y.; Seshadri, R.; Cheetham, A. K. Perovskite-Related ReO_3-Type Structures. *Nat. Rev. Mater.* **2020**, *5* (3), 196−213.
(48) Klimczuk, T.; Walker, H. C.; Springell, R.; Shick, A. B.; Hill, A. H.; Gaczyński, P.; Gofryk, K.; Kimber, S. A. J.; Ritter, C.; Colineau, E.; Griveau, J.-C.; Bouëxière, D.; Eloirdi, R.; Cava, R. J.; Caciuffo, R. Negative Thermal Expansion and Antiferromagnetism in the Actinide Oxypnictide NpFeAsO. *Phys. Rev. B: Condens. Matter Mater. Phys.* **2012**, *85* (17), 174506.
(49) Wang, J.; Sun, C. W.; Gong, Y. D.; Zhang, H. R.; Alonso, J. A.; Fernández-Diaz, M. T.; Wang, Z. L.; Goodenough, J. B. Imaging the Diffusion Pathway of Al^{3+} Ion in NASICON-Type $(Al_{0.2}Zr_{0.8})_{20/19}Nb(PO_4)_3$ as Electrolyte for Rechargeable Solid-State Al Batteries. *Chin. Phys. B* **2018**, *27* (12), 0−6.
(50) Belo, J. H.; Pires, A. L.; Gomes, I. T.; Andrade, V.; Sousa, J. B.; Hadimani, R. L.; Jiles, D. C.; Ren, Y.; Zhang, X.; Araújo, J. P.; Pereira, A. M. Giant Negative Thermal Expansion at the Nanoscale in the Multifunctional Material $Gd_5(Si, Ge)_4$. *Phys. Rev. B: Condens. Matter Mater. Phys.* **2019**, *100* (13), 134303.
(51) Flores, E.; Ares, J. R.; Castellanos-Gomez, A.; Barawi, M.; Ferrer, I. J.; Sánchez, C. Thermoelectric Power of Bulk Black-Phosphorus. *Appl. Phys. Lett.* **2015**, *106* (2), 12−16.
(52) Francisco, L. H.; Rodrigues, J. E.; Correr, W. R.; Hernandes, A. C. Blocking Effect in Promising Proton Conductors Based on $Ba_3Ca_{1.18}Nb_{1.82-x}R_xO_{9-\delta}$ (R = Y^{3+}, Gd^{3+}, Sm^{3+}, Nd^{3+}) Ordered Perovskites for PC-SOFCs. *Ceram. Int.* **2018**, *44* (9), 10806−10812.
(53) Goldsmid, H. J.; Sharp, J. W. Estimation of the Thermal Band Gap of a Semiconductor from Seebeck Measurements. *J. Electron. Mater.* **1999**, *28* (7), 869−872.
(54) Zevalkink, A.; Smiadak, D. M.; Blackburn, J. L.; Ferguson, A. J.; Chabinyc, M. L.; Delaire, O.; Wang, J.; Kovnir, K.; Martin, J.; Schelhas, L. T.; Sparks, T. D.; Kang, S. D.; Dylla, M. T.; Snyder, G. J.; Ortiz, B. R.; Toberer, E. S. A Practical Field Guide to Thermoelectrics: Fundamentals, Synthesis, and Characterization. *Appl. Phys. Rev.* **2018**, *5* (2), No. 021303.

https://dx.doi.org/10.1021/acs.inorgchem.0c01573
Inorg. Chem. XXXX, XXX, XXX−XXX